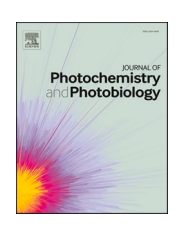
ELSEVIER

Contents lists available at ScienceDirect

# Journal of Photochemistry and Photobiology

journal homepage: www.sciencedirect.com/journal/journal-of-photochemistry-and-photobiology





# Are the emission quantum yields of cesium plumbobromide perovskite nanocrystals reliable metrics for their quality?

Jesse Tamayo a,f, Tori Do b,g, Karen El-Maraghy b,h, Valentine I. Vullev a,c,d,e,\*

- <sup>a</sup> Department of Chemistry, University of California, Riverside, CA 92521, USA
- <sup>b</sup> Department of Cell Biology and Neuroscience, University of California, Riverside, CA 92521, USA
- <sup>c</sup> Department of Bioengineering, University of California, Riverside, CA 92521, USA
- <sup>d</sup> Department of Biochemistry, University of California, Riverside, CA 92521, USA
- e Materials Science and Engineering Program, University of California, Riverside, CA 92521, USA.
- f Department of Chemistry and Physics, Santa Rosa Junior College, Santa Rosa, CA 95401, USA.
- g School of Nursing, Johns Hopkins University, 525 N Wolfe St, Baltimore, MD 21205, USA.
- <sup>h</sup> School of Nursing and Health Professions, University of San Francisco, San Francisco, CA 94117, USA.

#### ARTICLE INFO

# Key words: Cesium lead bromide CsPbBr<sub>3</sub> Perovskite synthesis Time-resolved emission spectroscopy Poisson distribution

#### ABSTRACT

The impact of halide perovskites on photonics, optoelectronics and energy science is indisputable. The pursuit of perovskite nanomaterials has open roads for explorations where large surface-to-volume ratios are paramount. While the solution-phase synthesis of most nanoparticles is relatively easy, the cleaning steps for obtaining populations of high-quality nanocrystals in good yields tend to present some challenges. As an extensive number of reports show, the quality of photoluminescent nanoparticles usually correlates with increased optical-emission quantum yields. Herein, we examine the products from the cleaning steps, involving centrifugation and resuspension washes, of an established procedure for preparing cesium plumbobromide nanocrystals. The photoluminescence quantum yields of the collected nanocrystals drops by about 10% to 30% after each wash. At the same time, the average exciton lifetime increases by about a factor of four, which reflects a decrease in the radiative-decay rates by about factor of five, while the non-radiative ones increase by less than a factor of two. Further analysis indicates that decreasing the particles size, along with changing their morphology, alters some of the exciton traps, or "quenching" sites, on them. This size decrease, along with changes that accompany it, shorten the exciton lifetimes while enhancing the limited spatial overlap between the holes and the electrons of the excitons and considerably increasing the radiative rates of deactivation. These findings do not suggest that good quality nanoparticles should not necessarily manifest high emission quantum yields. Rather, they point to the complexity of nanomaterials, due to their inherent heterogeneity, that warrants multimodal analysis for understanding the exciton dynamics, while correlating it to observed structural characteristics.

### 1. Introduction

Lead and tin halide perovskites have attracted considerable attention in the past decade due to their immensely promising performance not only as photovoltaic (PV) media, but also as light-emitting materials, photodetectors, and photocatalysts [1–6]. Calcium titanate perovskite, CaTiO $_3$ , is a rare mineral in the Earth's crust, which was first discovered in the Ural Mountains by Gustav Rose in 1839 and was named after his contemporary, Count Lev Alekseyevich von Perovskiy (Граф фон Перовский) who was also a mineralogist and a pioneer in the founding of the Russian Geological Society. Consequently, "perovskite" has evolved

as a general term for compounds with stoichiometries, such as  $A^{x+}B^{y+}X^{z-}_3$  with 3z = x + y (and derivatives of it with three cations and two anions), that adopt the crystal structure of the natural CaTiO<sub>3</sub>. Swapping the positions of the cations and the anions in these structures leads to inverse perovskites, or antiperovskites, such as Li<sub>3</sub>OX (X = halides), which in their own terms have promising electrical properties [7].

First synthesized by Wells at the end of the 19<sup>th</sup> century [8] and further studied by Møller in the 1950s [9, 10], lead halide perovskites have open new possibilities for photonics and electronics [11]. The expansion to tin and germanium analogues [12, 13], while promising, proved challenging due to chemical stability issues when exposed to air.

E-mail address: vullev@ucr.edu (V.I. Vullev).

 $<sup>^{\</sup>ast}$  Corresponding author.

After all, while the reduction potentials of lead (IV) compounds,  $E_{\text{Pb}(\text{IV})|}$   $_{\text{Pb}(\text{II})}$ , are around 1.5 V vs. SCE and larger, ensuring that  $\text{Pb}^{2+}$  is relatively stable in oxidizing atmosphere,  $E_{\text{Sn}(\text{IV})|\text{Sn}(\text{II})} \lesssim 0$  V vs. SCE and  $E_{\text{Ge}(\text{IV})|\text{Ge}(\text{II})} \lesssim -0.5$  V vs. SCE, making it challenging to prevent the oxidation of  $\text{Sn}^{2+}$  and especially of  $\text{Ge}^{2+}$ .

Goldschmidt tolerance factor,  $\alpha$ , used originally for quantifying the stability of ABO<sub>3</sub> perovskites from the effective radii of the comprising ions,  $r_A$ ,  $r_B$  and  $r_X$ , allows quantifying the structural stability of ABX<sub>3</sub> structures [14]:

$$\alpha = \frac{(r_{\rm A} + r_{\rm X})}{\sqrt{2}(r_{\rm B} + r_{\rm X})} \tag{1a}$$

where the values for the effective ionic radii are extracted from known crystal structures, considering the interionic distances in the lattices, along with the volume, the state of oxidation and the coordination number of each ion [15]. Indeed, using different databases and estimates of the ionic radii in eq. 1a produces variations in the values of  $\alpha$  reported for the same perovskite materials [16–18].

In his original publication, Goldschmidt used  $\alpha$  to designate the ratio in eq. 1a, but in the current literature t and  $\tau$  are also widely used.

Ideally,  $\alpha$  should assume values as close as possible to 1 for a stable cubic lattice; and as  $\alpha$  exceeds 1.1 or drops below 0.9, orthorhombic, tetragonal and monoclinic structures may emerge [10, 14]. In addition to  $\alpha$ , an octahedral factor ( $\mu$ ) accounts for the stability of the arrangement of the [B  $^{y+}$ X $^{z-}$ 3] $^{y-3z}$  units in the perovskite crystal lattice [17]:

$$\mu = \frac{r_{\rm B}}{r_{\rm x}} \tag{1b}$$

Values of  $\mu$  between 0.44 and 0.90 broaden the range of the Goldschmidt tolerance factor, warranting stable perovskite structures with compositions with 0.81 <  $\alpha$  < 1.11 [19]. For CsPbBr<sub>3</sub>, for example, the reported values of  $\alpha$  range between about 0.81 and 0.86 and  $\mu$  is in the order of 0.66 [16–18], which not only makes it one of the most stable perovskite structures, but also permits tolerance for doping and alloying with other ions, such as Rb<sup>+</sup> and Ag<sup>+</sup>, in the pursuit of compositions with enhanced photoluminescence quantum yield ( $\phi_{\rm PL}$ ) [18, 20-22].

The Weber's discovery of organic-inorganic hybrid perovskites in the 1970s, with methylammonium serving as  $A^+$  [23, 24], provided the platform for the work from Mitzi *et al.* in the 1990s [25], and the 2009 breakthrough by Miyasaka *et al.* demonstrating the utility of perovskite materials for PV devices [26]. These initial steps, which followed more than 100-years of research developments, triggered the fastest known evolution in the performance of PV devices of any class. In less than a decade, the power-conversion efficiency of perovskite solar cells grew from about 3.8% to more than 20% [26–28].

The impact of the hybrid perovskites on the impressive development of the field is indisputable. Recently, however, the interest is shifting back to all inorganic lead halide perovskites due to their relatively high stability and durability. This trend is especially pronounced in the development of perovskite nanomaterials, where the surface-to-volume ratios are inherently large [29–31]. A range of strategies, involving ion doping, modification of the surface coatings and encapsulation in different materials, improve not only the stabilize of perovskite nanocrystals (NCs), but also their photoluminescence quantum yields,  $\phi_{\rm PL}$  [29].

The emission quantum yield,  $\phi_{PL}$ , serves as a key criterion for the quality of photonic nanomaterials. As important as the luminescence efficacy is for a wide range of applications, such as light-emitting devices, the complexity of perovskite nanomaterials warrants caution when using  $\phi_{PL}$  as an "one dimensional" test of their quality. It is practically a "trademark," for example, for the emission wavelength of the NCs composed of direct-bandgap chalcogenides of the second analytical group of cations to strongly depend on the size, allowing tuning the PL of the same material from the ultraviolet to the near-infrared spectral regions by only varying the particle size. Conversely,

the size of perovskite NCs does not have such a dramatic effect on their optical bandgaps and luminescence output. The size of readily achievable stable NCs, composed of halide perovskites, usually exceeds their Bohr diameters, making the bandgap insensitive to the size of the particles. Therefore, perovskite cubic NCs with edge size in the order of 10 nm and larger are not truly quantum dots. On the other hand, changes in the chemical composition allows for tuning the PL wavelengths from the blue to the red regions of the spectrum [32, 33]. Variations in composition, morphology and coatings of perovskite nanomaterials alter their emission quantum yields over an order of magnitude, as evident from reported  $\phi_{PL}$  values that can be smaller than 0.1 in some cases and approach unity in others [32–39]. An increase in  $\phi_{PL}$  originates from enhancing the radiative and suppressing the non-radiative pathways of exciton deactivation. Thus, deterioration of the quality of NCs that accompanies an introduction of sites with improved oscillator strength, may still lead to an increase in  $\phi_{PL}$  while shortening the exciton lifetimes. This photophysical feature, along with the inherent heterogenous nature of the exciton-deactivation kinetics, makes emission quantum yields a necessary but not sufficient characteristic for evaluating the quality of photonic nanomaterials.

As relatively simple as the synthesis of lead halide perovskite NCs can be, their separation from the reaction mixture and purification warrants a great deal of caution. Upon completion of the synthesis and bringing the reaction mixture to room temperature, a series of centrifugation and resuspension washing steps can yield NC samples with high quality [32, 40]. Perovskites are notoriously susceptible to moisture and polar media. Even moderately polar solvents, such as chloroform and tetrahydrofuran, can readily alter the morphology, or completely dismantle, perovskite NCs [40, 41]. This inherent susceptibility of halide perovskites to polar media places a conundrum regarding the solvents for the centrifugation-resuspension wash steps. The solvents have to be strong enough to readily dissolve the unreacted oleic salts, such as lead oleate and oleylammonium halide, but weak enough to ensure it does not compromise the fidelity of the synthesized NCs.

Herein, we focus on the changes in the populations of CsPbBr $_3$  NCs after each centrifugation-resuspension wash step. After the initial precipitation of the NCs from the reaction mixture with a strong solvent, such as acetone, we use benzene for the following wash steps and collected the obtained supernatant suspensions after each centrifugation step. High emission quantum yield,  $\phi_{PL}$ , is a key indication for the quality of the NCs. The  $\phi_{PL}$  of the NCs in the collected supernatants decreases after each wash. Concurrently, the NC morphology improves after the first benzene wash, as electron micrographs reveal; and the lifetimes obtained from photoluminescence decays of the NCs also increase significantly after the first benzene wash. These findings indicate that improving the quality of such nanomaterials (i.e., attaining population of predominantly cuboidal particles with a similar size) enhances their exciton lifetimes, while decreasing the rates of radiative deactivation.

# 2. Experimental

## 2.1. General information

The reagents for the synthesis were purchased from Millipore Sigma and used as received. The solvents, dry for electrochemistry, and spectroscopic grade for optical measurements, were obtained from Thermo Fisher Scientific. The deuterated benzene,  $C_6D_6$ , for the NMR studies was purchased from Sigma Aldrich Inc. Micrographs were recorded using a Tecnai12 transmission electron microscope [42–44]. The sample solutions were diluted for adequate dispersion of the nanoparticles on carbon 400 mesh grids. The recorded images were contrasted to highlight the edges of each particle. ImageJ allowed estimating the dimensions of at least a hundred particles for each sample from different images recorded for the suspension obtained from multiple synthesis trials. Proton NMR spectra were recorded using a Bruker Avance 500 MHz

spectrometer [45, 46]. The proton chemical shift of the traces of  $C_6D_5H$ , 7.16 ppm, served as an internal standard.

#### 2.2. Synthesis

We adapted a previously published procedure for the synthesis of the CsPbBr<sub>3</sub> NCs [32]. To produce cesium oleate, Cs<sub>2</sub>CO<sub>3</sub> (81 mg, 0.25 mmol) and oleic acid (0.25 mL, 0.8 mmol) were suspended in 4 mL 1-octadecene and stirred at 110 °C for 1 hour under vacuum prior to placing it under nitrogen. In parallel, PbBr<sub>2</sub> (69 mg, 0.19 mmol) was suspended in 5 mL 1-octadecene and also stirred at 110 °C for 1 hour under vacuum and blanked with nitrogen. Oleic acid (0.5 mL, 0.16 mmol) and oleylamine (0.5 mL, 0.15 mmol) were injected in the PbBr<sub>2</sub> suspension and the temperature of the mixture was elevated to 150 °C. Concurrently, the temperature of the cesium oleate solution was elevated to 180  $^{\circ}$ C. A quick injection of some of the hot cesium oleate solution (0.4 mL) into the vigorously stirred PbBr<sub>2</sub> mixture resulted in the formation of yellow suspension with greenish luminescence. During the hot-injection and stirring, the nanocrystals form while the oleylamine and the oleic acid coat them to maintain their structural integrity and colloidal stability in hydrocarbon solvents. Immediately after the vellow coloration and the appearance of the green fluorescence, the reaction mixture was cooled down in a water bath. Addition of 1 mL acetone to the cooled mixture and centrifugation at 10,000 rpm for 3 minutes resulted the formation of a yellow pellet that was collected and resuspended in 0.6 mL dry benzene. This solution was centrifuged for 30 seconds at 10,000 rpm and the supernatant (SN1) was collected for further studies. (A series of tests revealed that 30 s is the shortest centrifugation time, at 10,000 rpm, after which the benzene supernatant is not cloudy.) The pellet was resuspended again in 0.6 mL dry benzene and centrifuged to produce the second supernatant suspension (SN2). Repeating this resuspension/centrifugation procedure once again yielded the third suspension (SN3). It should be noted, that while we use dry benzene blanketed with argon for the washing steps, the procedures are carried out under ambient conditions, which exposes the solutions to the humidity of the laboratory atmosphere. The optical steady-state spectra of the prepared samples, however, remain unperturbed for about one to two weeks. Nevertheless, for these studies, we use samples that are prepared within 24 hour of each of the measurements.

# 2.3. Optical spectroscopy

Steady-state absorption spectra are recorded in a transmission mode using a JASCO V-670 spectrophotometer (Tokyo, Japan). The steady-state emission spectra and the time-correlated single-photon counting (TCSPC) fluorescence decays are measured, using a FluoroLog-3 spectrofluorometer (Horiba-Jobin-Yvon, Edison, NJ, USA), equipped with a pulsed diode laser ( $\lambda=406$  nm, 200-ps pulse full width at half maximum, FWHM) and a TBX detector [47–49]. Recording the TCSPC photoluminescence decays at a frequency of 100 kHz and less, ensures a complete deactivation of the exciton emission after each pulse. All samples are transferred into 1-cm square quartz cuvettes with four polished sides equipped with screw caps and septa, and are purged with argon for 5 to 10 min per 1 mL of solution prior to each measurement.

The photoluminescent quantum yields,  $\phi_{PL}$ , are determined by comparing the integrated emission intensities of the samples,  $I(\lambda)$ , with the integrated fluorescence of a reference sample,  $I_0(\lambda)$ , with a known fluorescence quantum yield,  $\phi_0$  [50]:

$$\varphi_{\rm PL} = \varphi_0 \frac{\int I(\lambda) d\lambda}{\int I_0(\lambda) d\lambda} \frac{1 - 10^{-A_0(\lambda_{\rm ex})}}{1 - 10^{-A(\lambda_{\rm ex})}} \cdot \frac{n^2}{n_0^2}$$
(2)

where  $A(\lambda_{ex})$  is the absorbance at the excitation wavelength; and n is the refractive index of the media. The subscript "0" indicates the quantities for the used reference sample. We employed alkaline aqueous solutions (pH = 10) of fluorescein as reference samples,  $\phi_0 = 0.93$  [51, 52],  $\lambda_{ex} = 0.93$ 

470 nm, and  $(n \ n_0^{-1})^2 \approx 1.27$ . For the emission-quantum yield measurements, the absorption of the samples and the reference at the excitation wavelengths is kept between 0.1 and 0.2 and the spectra are emission signal is collected at a 90° angle in relevance to the excitation beam.

For the time-correlated single-photon counting (TCSPC) emission-decays measurements, we use the same spectrofluorometer that we use for recording the steady-state spectra, but with the TBX detector running in a single-photon-counting mode [53]. Placing selected reflection neutral-density filters in front of the laser source controls the intensity of the excitation light. For recording the time-profile of the excitation pulse, we use the signal from the Rayleigh scattering from deionized water by tuning the emission monochromator to the excitation wavelength, i.e., 406 nm. For the emission decay, we tune to wavelengths corresponding to the luminescence bands we analyze.

#### 3. Results and Discussion

Adopting previously reported procedures [32], we prepare CsPbBr<sub>3</sub> perovskite nanocrystals (NCs) that assume cubic shapes (Figure 1,2). Rapid injection of a hot solution of lead bromide, PbBr<sub>2</sub>, oleic acid,  $C_{17}H_{33}CO_2H$ , and oleylamine,  $C_{18}H_{35}NH_2$ , into a heated vigorously stirred solution of freshly prepared cesium oleate,  $C_{3}(C_{17}H_{33}CO_2)$ , affords yellow suspension of perovskite NCs with distinct green photoluminescence (PL). An aliphatic hydrocarbon with a high boiling point, 1-octadecene ( $C_{18}H_{36}$ ), serves as a solvent for each of the solutions in this procedure. Employing polar solvents, such as *N*,*N*-dimethylformamide (which is thermally unstable), can lead to NCs with different stoichiometry and structure, such as round nanoparticles with decreased content of PbBr<sub>2</sub>, i.e.,  $C_{34}PbBr_{6}$  [40]. Conversely, treating CsPbBr<sub>3</sub> perovskite NCs with methanol depletes their CsBr content to produce nanoparticles of CsPb<sub>2</sub>Br<sub>5</sub> [41].

While using polar solvents in the separation and purification steps is unavoidable, we limit the exposure of the NCs to such potentially detrimental media to as short as possible durations. Adding acetone to the rapidly cooled reaction mixture precipitates the NCs, while providing sufficient solubility of most of the labile organic components. Centrifugation allows us to collect the NCs as pellets, which we resuspend in benzene and centrifuge again to remove a portion of the nanoparticles and collect the supernatant, i.e., SN1. Repeating this resuspension-centrifugation step two more times, allows to collect the supernatants, i.e., SN2, and SN3, for further analysis and comparison. Further resuspension-centrifugation step produce supernatants suspension containing heterogeneous populations of NCs, many with sizes exceeding 30 nm.

The first wash step with benzene makes the biggest difference in the consistency of the NC suspensions. The optical absorption and photo-luminescence maxima of SN2 are bathochromically shifted by 9 and 4 nm, respectively, in comparison with those of SN1 (Figure 3, Table 1). The PL band of SN1 is about 14% to 19% wider than the emission bands of SN2 and SN3, respectively, as the full widths at their half maxima (FWHM) reveal (Table 1). Conversely, the differences between the spectral maxima of SN2 and SN3 is about 1 nm. Concurrently, while the photoluminescence quantum yield,  $\phi_{\rm PL}$ , of SN1 is close to quantitative,  $\phi_{\rm PL}$  of SN2 and SN3 drops to about 0.7 (Table 1). Also, the FWHM of the PL bands of SN2 and SN3 are practically the same (Table 1).

The morphology of the NCs in the different suspensions reflects the differences that their optical properties reveal. SN1 contains a relatively monodispersed population (8.2  $\pm$  0.6 nm) of NCs that do not all have well-defined cuboidal shape, characteristic for the CsPbBr3 perovskite (Figure 1a, 2a). Furthermore, SN1 is substantially loaded with C $_{18}H_{36}$  and C $_{17}H_{33}CO_2H$  / C $_{18}H_{35}NH_2$  in comparison with SN2 and SN3, as their NMR spectra reveal (Figure 4). The inhomogeneity in the NC shapes and the abundance of non-volatile organic material precludes the NCs from forming orderly packed films on the TEM sample holder. In contrast, SN2 contains cuboidal NCs that self-assemble in monolayered films

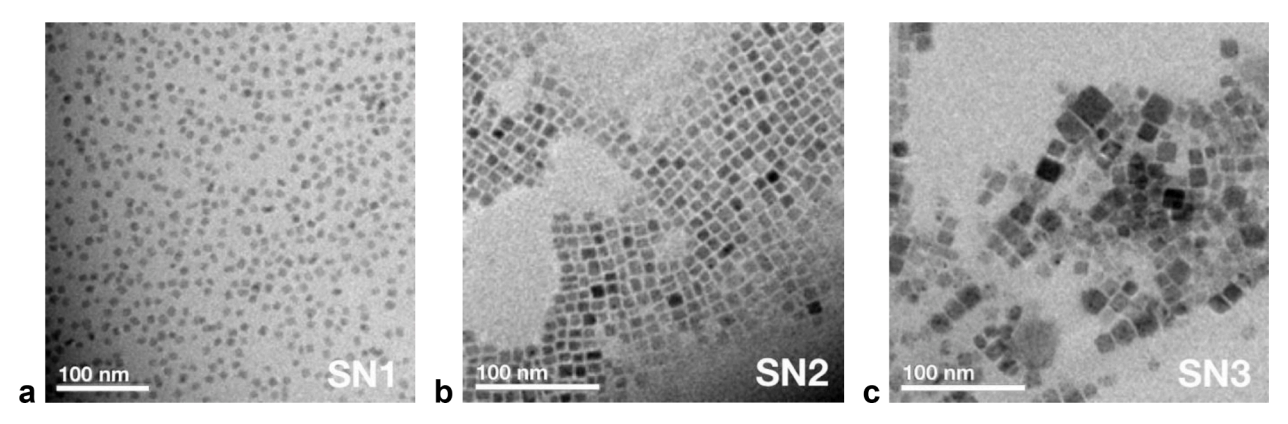
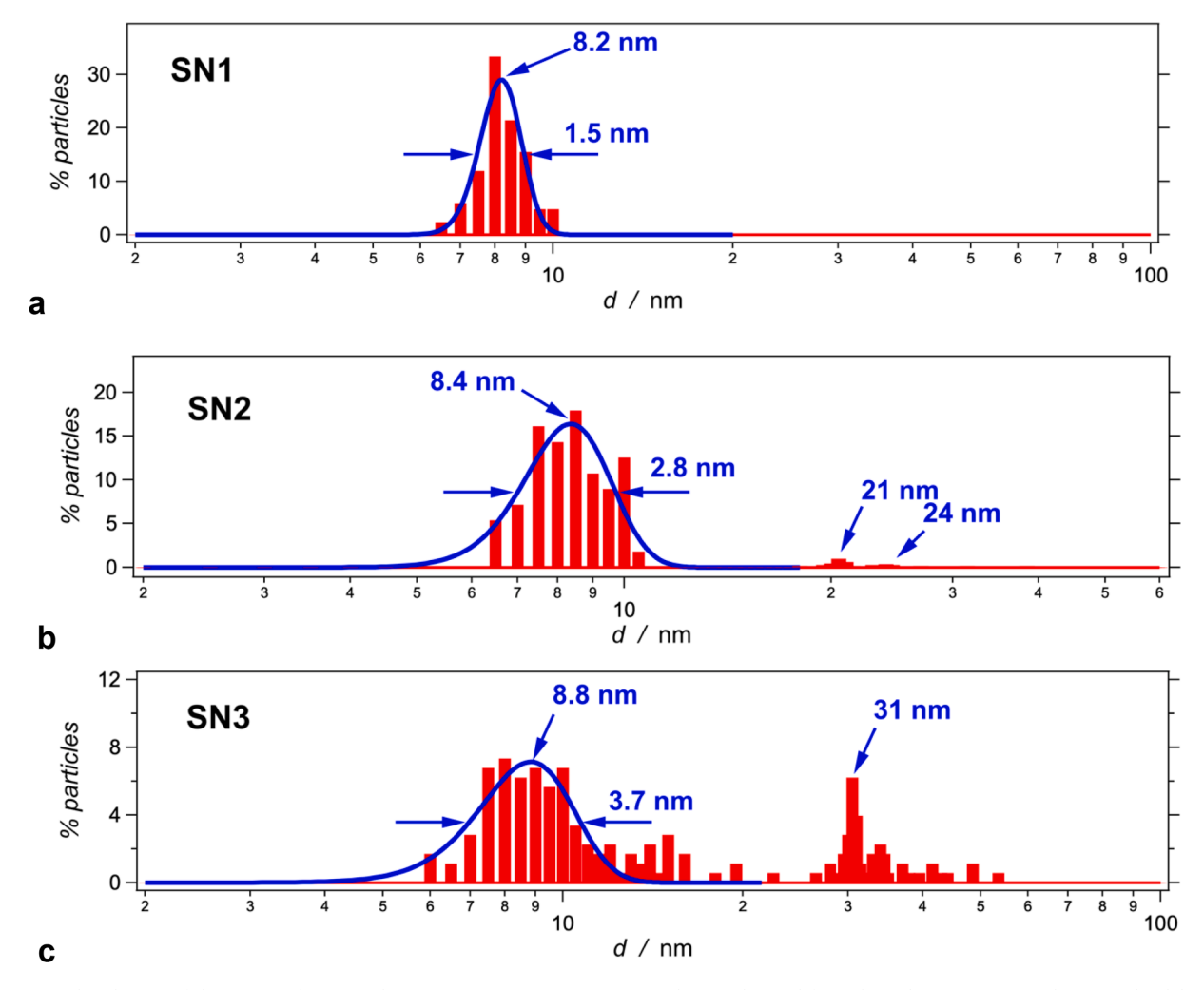


Figure 1. Electron micrographs of dried benzene supernatants, SN1, SN2 and SN3, collected after the centrifugations following different washes of the synthesized cesium plumbobromide nanoparticle: (a) SN1 – supernatant collected after centrifugation of the resuspended (in benzene) acetone-induced precipitation from the crude reaction mixture; (b) SN2 – supernatant collected after centrifugation of SN1; and (c) SN3 – supernatant collected after centrifugation of SN2. The images indicating that while the first benzene wash is key for collecting cesium plumbobromide particles with cuboidal morphology (in the SN2 suspension), further washes enhance the NC population with large particles.



**Figure 2.** Size distribution of the NC populations in benzene supernatants, SN1, SN2 and SN3, obtained from their electron micrographs. For cuboidal particles, d represents the average of lengths of the visible edges, and for rounded particles, d represents the diameter of the circles in which they fit. The blue lines represent the Gaussian fits of the populations with d < 20 nm, with the maxima and the full widths at half maxima designated.

when their suspension dry on the TEM sample holders (Figure 1b). The sizes of the SN2 NCs, however, is not as monodispersed as that of SN1, and is shifted toward larger values (Figure 2b). The size distribution of the SN3 NCs shows even worse monodispersity than that of SN2

(Figure 3c). In addition to the 9-nm NCs that appear similar to those of SN2, SN3 contains a substantial population of large cuboidal particles (Figure 2c). While the NCs in SN2 and SN3 have more heterogeneous size distribution than the NCs in SN1, the SN2 and SN3 show slightly

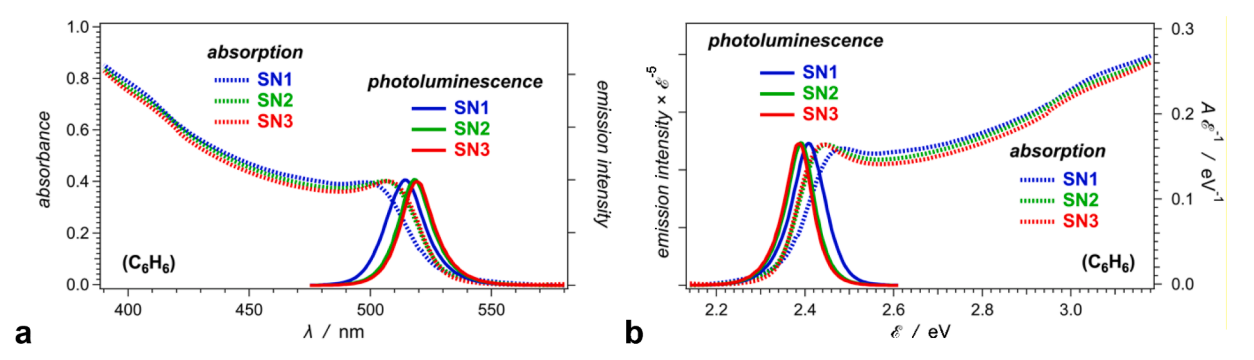


**Figure 3.** Optical absorption and emission spectra of benzene supernatants, SN1, SN2 and SN3, plotted against (a) wavelength and (b) energy after transition-dipole moment corrections, i.e.,  $A(\mathcal{E}) = A(\lambda) \mathcal{E}^{-1}$  and  $PL(\mathcal{E}) = PL(\lambda) \mathcal{E}^{-5}$  [61]. The concentrations were adjusted to give similar absorbance at the maxima around 500 nm, i. e., at the bathochromic edges of the spectra. The photoluminescence spectra are normalize to their maxima ( $\lambda_{ex} = 470 \text{ nm}$ ).

Table 1
Photophysical characteristics of the NCs in supernatants SN1, SN2 and SN3.

		-	
	SN1	SN2	SN3
$\lambda(A_{max})$ / nm <sup>a</sup>	$497 \pm 2$	$506\pm1$	$507\pm1$
$\lambda(PL_{max})$ / nm <sup>a</sup>	$514\pm1$	$518\pm1$	$519\pm1$
$\mathscr{E}(A_{max})$ / eV <sup>a</sup>	$2.48\pm0.02$	$2.45\pm0.01$	$2.44\pm0.02$
$\mathscr{E}(PL_{max})$ / eV $^{a}$	$2.41\pm0.02$	$2.39 \pm 0.01$	$2.39\pm0.01$
Δ € / meV <sup>b</sup>	$70\pm30$	$60\pm10$	$50\pm20$
$FWHM_{PL}  /  meV$	$87\pm5$	$76\pm3$	$73\pm4$
С			
$\phi_{ m PL}$	$0.95\pm0.10$	$0.75\pm0.15$	$0.70\pm0.12$
$\tau_1$ / ns $(\alpha_1)^{d}$	3.63 (0.8365)	3.82 (0.845)	4.83 (0.808)
$\tau_2$ / ns $(\alpha_2)^{d}$	12.3 (0.1559)	14.5 (0.137)	18.2 (0.172)
$\tau_3$ / ns $(\alpha_3)^{\rm d}$	44.6 (0.0072)	71.6 (0.015)	74.7 (0.017)
$\tau_4$ / ns $(\alpha_4)^{d}$	244 (0.0004)	309 (0.003)	304 (0.003)
$\tau_5$ / ns $(\alpha_4)^{\rm d,e}$	$>$ 1,000 $^{\mathrm{b}}$ (3 $ imes$	$>$ 1,000 $^{\rm b}$ (2 $ imes$	$>$ 1,000 $^{\rm b}$ (3 $ imes$
	$10^{-5}$ )	$10^{-5}$ )	$10^{-5}$ )
$\chi^{2f}$	1.26	1.09	0.94
$d^{\mathrm{f}}$	2.02	2.04	1.92
$\overline{\tau}$ / ns <sup>g</sup>	13.9	52.3	49.7
$k_{ m PL}_{ m h}  imes 10^{-6} \ / \ { m s}^{-1}$	68	14	14
$k_{\substack{\text{nd} \\ \text{h}}} \times 10^{-6} / \text{ s}^{-1}$	3.6	4.8	6.0

<sup>&</sup>lt;sup>a</sup> Absorption (at the bathochromic edges of the spectra) and photoluminescence maxima extracted from spectra plotted against wavelength and energy (Figure 3).

narrower PL spectral bands than SN1 (Table 1, Figure 2). These findings suggest that most likely the principal contribution to spectral broadening originates from irregularly shaped NCs with sizes comparable to or smaller than the exciton Bohr diameter, which for perovskite  $CsPbBr_3$  is about 7 nm [32].

The PL decays reveal somewhat an unusual trend. While  $\varphi_{\rm PL}$  decreases after each wash, the exciton lifetimes appear to increase

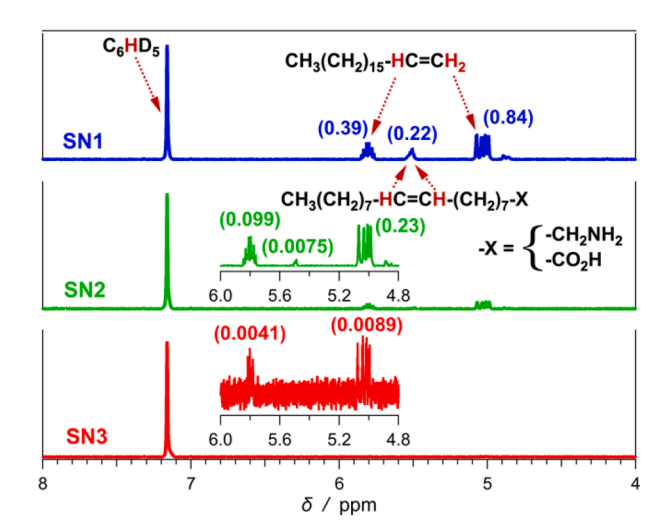


**Figure 4.** Alkene and aromatic regions of the  $^1\text{H}$  NMR spectra of the content of supernatants SN1, SN2 and SN3, adjusted to have optical absorption of 0.5 at 500 nm in a 1-mm cuvette. After measuring the absorption, 1 mL of each sample was dried under vacuum and redissolved in 1 mL  $C_6\text{HD}_5$  for the NMR measurements. The spectra show the signals from the alkene protons of oleyl amine and/or oleic acid, which overlap when bound to perovskite NCs, along with abundance of the non-volatile solvent, 1-octadecane, used for the synthesis, which always accompanies NCs synthesized using such a procedure, as previously reported [62]. The values in the parentheses represent the integrated area under each peak divided by the integrated area of the solvent peak at 7.16 ppm.

(Figure 5). Multiexponential fits show an increase in all time constants,  $\tau_i$ , after the first benzene wash, and the intensity-average lifetime,  $\bar{\tau}$ , of SN2 exceeds  $\bar{\tau}$  of SN1 by more than a factor of three (Table 1). As a result, the average radiative-decay rate constant,  $k_{\rm PL}$ , of SN1 is more than four times larger than  $k_{\rm PL}$  of SN2 and SN3, while the non-radiative decay rate constants,  $k_{nd}$ , differ by less than a factor of two (Table 1). That is, the spatial overlap between the hole and the electron orbitals of the excitons in the NCs, allowing transitions with minimum phonon coupling, governs the observed photophysical tends. The slightly larger NC size in SN2 and SN3, in comparison with SN1, could offer a rationale for the  $k_{\rm PL}$  trends. The sizes of these particles, however, exceed the 7-nm effective Bohr diameter estimated for CsPbBr<sub>3</sub> [32].

Despite the broad use of multiexponential fits for analyzing PL decays of nanoparticles, the interpretation of the results should be approached with a certain level of caution. Such fitting function, indeed, reflect the inherent heterogeneous nature of samples of luminescent NCs. This heterogeneity, however, can originate from: (1) differences in size and shape of the NCs in the sample; and (2) different defects and

<sup>&</sup>lt;sup>b</sup> Stokes' shifts,  $\Delta \mathscr{E} = \mathscr{E}(A_{max}) - \mathscr{E}(PL_{max})$ .

<sup>&</sup>lt;sup>c</sup> Full widths at the half maxima (FWHM) of the photoluminescence bands.

<sup>&</sup>lt;sup>d</sup> Lifetimes,  $\tau_i$ , along with the normalized amplitudes,  $\alpha_i$ , obtained from multiexponential data fits,  $I_{PL}(t) = \sum_i \alpha_i \exp(-t \tau_i^{-1})$  [54, 55].

 $<sup>^</sup>e$  While tetraexponential functions do not provide good fit for the microsecond regions of the decays,  $\tau_5$  of pentaexponential fits for each decay converges to different values between about 1  $\mu s$  and 5  $\mu s$  depending on the initial input value.

<sup>&</sup>lt;sup>f</sup> Chi square ( $\chi^2$ ) tests of the goodness of the pentaexponential fits, and autocorrelation (d) tests, as implemented by the Durbin-Watson statistics, for examining the appropriateness of the fitting function [56–60].

 $<sup>^</sup>g$  Intensity-average lifetimes from the first four exponential components,  $\overline{T}=(\Sigma_i\alpha_i\tau_i^2)\,(\Sigma_i\alpha_i\tau_i)^{-1}$ .

<sup>&</sup>lt;sup>h</sup> Averagerate constants of radiative and non-radiative decay rate, i.e.,  $k_{PL}=\varphi_{PL}~\overline{\tau}^{-1}$  and  $k_{nd}=(1-\varphi_{PL})~\overline{\tau}^{-1}$ .

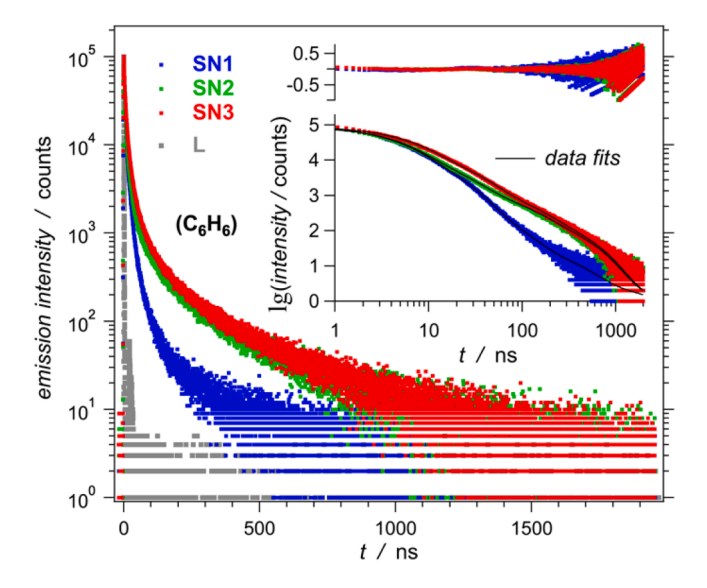


Figure 5. Photoluminescence decays of supernatants SN1, SN2 and SN3, obtained using time-correlated single photon counting (TCSPC). Instrument response to the laser excitation (L):  $\lambda_{\rm ex}=406$  nm and FWHM = 200 ps [63]. The inset shows the global fits of the decays (Table 2) along with the residuals. The logarithmic scale of the abscissa allows to illustrate the changes that span over three orders of magnitude. For reliability of the fits at  $t\gtrsim 500$  ns, where the intensity drops by more than three orders of magnitude, the data fits were carried out using the logarithm of the Poisson-distribution function (eq. 3), i.e.,  $\lg(I_{\rm PL}(t))$ . (Chi-square and Durbin-Watson tests for the goodness of the global fit yield:  $\chi^2=1.17$ ; d=1.91 [56–60].)

traps (within the bulk and on the surfaces of the particles) distributed of populations of NCs with identical shape and size. To account for the latter, we resort to a model that was initially developed for explaining micelle-mediated emission quenching, and assumes a Poisson distribution of each of several quenchers over the particles in the suspension [64, 65]. Assuming each quencher represents a different exciton trap in the nanoparticles has allowed the successful application of this model for the analysis of PL decays of quantum dots [66–72]. Adopting this model, allows representing the time-evolution of the emission intensity,  $I_{\rm PL}(t)$ , observed for suspensions containing m types of NCs with n different exciton traps distributed among them:

$$I_{PL}(t) = \sum_{i=1}^{m} I_{i,0} \exp\left(-\frac{t}{\tau_{i,0}} - \sum_{j=1}^{n} \left\langle N_{i,j} \right\rangle \left(1 - \exp\left(-\frac{t}{\tau_{i,j}^{(T)}}\right)\right)\right)$$
(3)

where  $I_{i,0}$  is the initial amplitude of the PL intensity for the  $i^{\text{th}}$  type of NCs;  $\tau_{i,0}$  is the lifetime of the excitons in the  $i^{\text{th}}$  type of NCs in the absence of any traps;  $\langle N_{i,j} \rangle$  is the average number of a type j traps per particle in the  $i^{\text{th}}$  type of NCs; and  $\tau_{i,j}^{(\text{TT})}$  characterizes the lifetime of an exciton in a type j trap in the  $i^{\text{th}}$  type of NCs.

This Poisson-distribution model (eq. 3) where we vary m and n between 1 and 5, offers a means for global fits (GFs) of the PL decays recorded for SN1, SN2 and SN3, where the lifetimes,  $\tau_{i,0}$  and  $\tau_{i,j}^{(T)}$ , are set the same for all three suspensions, while the preexponential amplitudes,  $I_{i,0}$  and  $\langle N_{i,j} \rangle$ , are allowed to fluctuate independently for each sample. Allowing any of  $\tau_{i,0}$  and  $\tau_{i,j}^{(T)}$  to adjust independently to different values for each decay does not improve the quality of the data fits, but can compromise the convergence of the least-squares iterations. Setting m=1 and n=4 describes well the PL decays of all three samples, employing the smallest number of fitting parameters (Figure 5, inset).

Temperature dependence of the photophysical properties of the NCs provides a means to characterize the trap states that the Poisson-distribution model (eq. 3) postulates. Heating SN2, for example, results in a significant decrease in its emission quantum yield, as well as in a slight hypsochromic shift in the PL maximum and broadening of the PL

band (Figure 6). While these results are consistent with temperature-enhanced access to exciton traps with decreased efficacy of radiative deactivation, their interpretation should be approached with a great deal of caution and treated as qualitative at best. Unfortunately, raising the temperature above ca. 30 °C induces irreversible changes in the PL properties of these NC samples, as revealed by the losses in  $\phi_{PL}$  and the irreversible spectral broadening upon heating and cooling cycles (Figure 6). Conversely, circulating the temperature between about 5 and 30 °C does not induce detectable irreversible changes within the duration of the measurements.

The GF analysis of the PL decays reveals two key features about the exciton dynamics (Table 2). (1) The inherent exciton lifetime,  $\tau_{i,0}$ , for trap-free cesium lead bromide NCs (with sizes slightly exceeding the Bohr diameter [32]) is in the order of a microsecond. It is consistent with the low-amplitude slow components,  $\tau_5$ , that the multiexponential fits produce (Table 1). (2) The samples with different average  $k_{PL}$ , i.e., SN1 vs SN2 and SN3 (Table 2), have different number of traps inducing exciton lifetimes between about 0.3 and 1  $\mu$ s, i.e.,  $\langle N_{1,1} \rangle$  and  $\langle N_{1,2} \rangle$ (Table 2). That is, SN1, which has larger  $\phi_{PL}$  and shorter average lifetimes,  $\bar{\tau}$ , than SN2 and SN3 (Table 2), has a noticeable population of traps inducing 300-ns exciton lifetime, i.e., for SN1  $\langle N_{1,2} \rangle > 3$ , and practically none of the 1- $\mu$ s ones, i.e.,  $\langle N_{1,1} \rangle < 0.05$  (Table 2). In contrast, the particles in SN2 and SN3 are practically depleted of traps that shorten the exciton lifetime to around 300 ns, i.e.,  $\langle N_{1,2} \rangle \lesssim 0.2$  for SN2 and  $\langle N_{1,2}\rangle \lesssim 0.1$  for SN3, while loaded with traps that induce lifetimes almost as long as  $\tau_{i,0}$ , i.e.,  $\langle N_{1,1} \rangle$  (SN2)  $\approx \langle N_{1,1} \rangle$  (SN3)  $\approx 5$  (Table 2). Therefore, the structural features in these all-inorganic lead halide NCs that prolong the exciton lifetimes, also decrease the spatial overlap between the exciton hole and electron, lowering the luminescence oscillator strength and the rates of radiative decay.

#### 4. Conclusions

While the synthesis of perovskite and other luminescent nanoparticles is relatively easy, their separation from the reaction mixture and purification is not always straightforward. The inherent structural heterogeneity of such nanomaterials renders the reproducibility of their preparation somewhat challenging. Electron microscopy is a primary tool for examining the morphology of the NC populations, and NMR

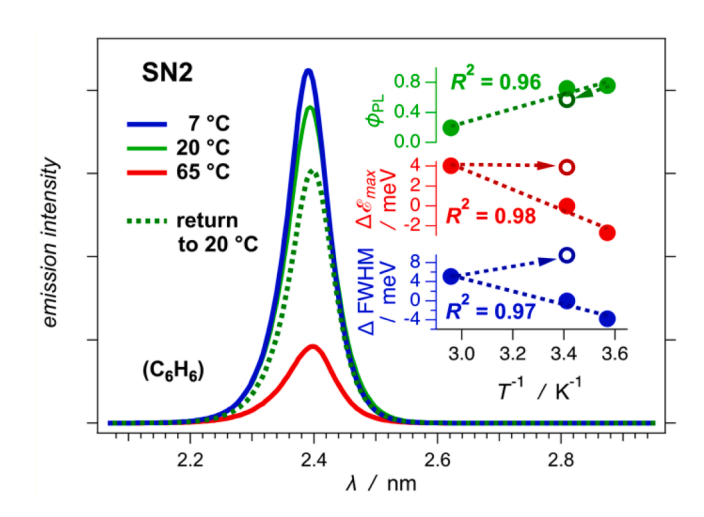


**Figure 6.** Temperature dependence of the PL properties of SN2, including thermal effects on: emission quantum yield,  $\phi_{PL}$ , spectral maxima, i.e.,  $\Delta \mathscr{E}_{max} = \mathscr{E}(\text{PL}_{max}) - \mathscr{E}(\text{PL}_{max}, 20 \, ^{\circ}\text{C})$ , and spectral widths, i.e.,  $\Delta \text{FWHM} = \text{FWHM} - \text{FWHM}(20 \, ^{\circ}\text{C})$ . The linear correlations ( $R^2$ ) are for the temperature increase from 7 to 65  $^{\circ}\text{C}$ , i.e., 280 to 338 K. An increase in temperature above about 30  $^{\circ}\text{C}$ , however, causes irreversible changes in the samples and cooling down does not recover the initial spectral properties. The spectrum depicted with the dashed dark green line and the hollow circular marker represent the PL properties after cooling down from 65 to 20  $^{\circ}\text{C}$ .

**Table 2** Outcomes of the global fits of the photoluminescence decays of the NCs in supernatants SN1, SN2 and SN3, using the Poisson-distribution model with m=1 and n=4 (eq. 3).

	SN1	SN2	SN3
$\tau_{1,0}$ / ns	$\textbf{1,410} \pm \textbf{450}$	$\textbf{1,410} \pm \textbf{450}$	$1{,}410 \pm 450$
$\tau_{1,1}^{(\mathrm{T})}$ / ns	$\textbf{1,070} \pm \textbf{230}$	$1{,}070\pm230$	$1,\!070\pm230$
$\tau_{1,2}^{(T)} / \text{ns}$	$311\pm72$	$311\pm72$	$311\pm72$
$\tau_{1,3}^{(T)} / \text{ns}$	$62.3 \pm 8.5$	$62.3 \pm 8.5$	$62.3 \pm 8.5$
$\tau_{1,4}^{(T)} / \text{ns}$	$15.5\pm1.4$	$15.5\pm1.4$	$15.5\pm1.4$
$\langle N_{1,1} \rangle$	$0.019\pm0.031$	$5.1\pm0.4$	$\textbf{5.4} \pm \textbf{0.2}$
$\langle N_{1,2}  angle$	$3.6\pm0.031$	$0.17\pm0.15$	$0.062 \pm 0.093$
$\langle N_{1,3}  angle$	$3.1\pm0.031$	$2.2\pm0.6$	$3.0 \pm 0.8$
$\langle N_{1,4}  angle$	$3.3\pm0.031$	$3.0\pm0.4$	$2.0\pm0.5$

spectroscopy – for monitoring the (free) organic components in the suspensions. It is optical spectroscopy, however, that provides key information about the electronic properties of such nanomaterials. Even then, the trends have layers of complexity that need examining. High photoluminescence quantum yields, for example, do not necessarily correlate with the exciton lifetimes and with the overall quality of the nanomaterials. Such considerations are crucial for designs of photonic, optoelectronic and solar-energy applications.

# **Declaration of Competing Interest**

The authors declare that they have no known competing financial interests or personal relationships that could have appeared to influence the work reported in this paper.

## Acknowledgements

The U.S.A. National Science Foundation funded this research (grant CHE 1800602, along with GRFP support for J. Tamayo).

#### References

- [1] Editorial, A decade of perovskite photovoltaics, Nat. Energy 4 (2019) 1.
- [2] L. Chouhan, S. Ghimire, C. Subrahmanyam, T. Miyasaka, V. Biju, Synthesis, optoelectronic properties and applications of halide perovskites, Chem Soc Rev 49 (2020) 2869–2885
- [3] M. Saliba, J.P. Correa-Baena, M. Grätzel, A. Hagfeldt, A. Abate, Perovskite Solar Cells: From the Atomic Level to Film Quality and Device Performance, Angew. Chem. Int. Edit. 57 (2018) 2554–2569.
- [4] M. Konstantakou, T. Stergiopoulos, A critical review on tin halide perovskite solar cells, J. Mater. Chem. A 5 (2017) 11518–11549.
- [5] H.W. Huang, B. Pradhan, J. Hofkens, M.B.J. Roeffaers, J.A. Steele, Solar-Driven Metal Halide Perovskite Photocatalysis: Design, Stability, and Performance, ACS Energy Lett 5 (2020) 1107–1123.
- [6] C. Han, X.L. Zhu, J.S. Martin, Y.X. Lin, S. Spears, Y. Yan, Recent Progress in Engineering Metal Halide Perovskites for Efficient Visible-Light-Driven Photocatalysis, ChemSusChem 13 (2020) 4005–4025.
- [7] Y.S. Zhao, L.L. Daemen, Superionic Conductivity in Lithium-Rich Anti-Perovskites, J. Am. Chem. Soc. 134 (2012) 15042–15047.
- [8] H.L. Wells, Über die Cäsium- und Kalium-Bleihalogenide (About the cesium and potassium lead halides), Z. anorg, allg. Chem. 3 (1893) 195–210.
- [9] C.K. Møller, Phase transition in CsPbCl3, Nature 180 (1957) 981-982.
- [10] C.K. Møller, Crystal structure and photoconductivity of cesium plumbohalides, Nature 182 (1958) 1436.
- [11] C.C. Stoumpos, M.G. Kanatzidis, Halide Perovskites: Poor Man's High-Performance Semiconductors, Adv. Mater. 28 (2016) 5778–5793.
- [12] G. Thiele, H.-W. Rotter, K.D. Schmidt, Kristallstrukturen und Phasentransformationen von Caesiumtrihalogenogermanaten(II) CsGeX3 (X = Cl, Br, I) (Crystal structures and phase transformations of cesium trihalogermanates CsGeX3 (X = Cl, Br, I)), Z. anorg. allg. Chem. 545 (1987) 148–156.
- [13] S.J. Clark, J.D. Donaldson, J.A. Harvey, Evidence for the direct population of solid-state bands by non-bonding electron pairs in compounds of the type CsMIIX3 (MII = Ge, Sn, Pb; X = Cl, Br, I), J. Mater. Chem. 5 (1995) 1813–1818.
- [14] V.M. Goldschmidt, Die Gesetze der Krystallochemie (The laws of chemical crystallography), Naturwissenschaften 14 (1926) 477–485.
- [15] R.D. Shannon, Revised effective ionic radii and systematic studies of interatomic distances in halides and chalcogenides, Acta Crystallogr., Sect. A A32 (1976) 751–767.

- [16] R.D. Shannon, Revised Effective Ionic-Radii and Systematic Studies of Interatomic Distances in Halides and Chalcogenides, Acta Crystallogr. A 32 (1976) 751–767.
- [17] C. Li, X. Lu, W. Ding, L. Feng, Y. Gao, Z. Guo, Formability of ABX3 (X = F, Cl, Br, I) halide perovskites, Acta Crystallogr., Sect. B: Struct. Sci. 64 (2008) 702–707.
- [18] D. Amgar, T. Binyamin, V. Uvarov, L. Etgar, Near ultra-violet to mid-visible band gap tuning of mixed cation RbxCs1-xPbX3 (X = Cl or Br) perovskite nanoparticles, Nanoscale 10 (2018) 6060–6068.
- [19] M.A. Green, A. Ho-Baillie, H.J. Snaith, The emergence of perovskite solar cells, Nat. Photonics 8 (2014) 506–514.
- [20] S. Ye, M. Yu, W. Yan, J. Song, J. Qu, Enhanced photoluminescence of CsPbBr3@Ag hybrid perovskite quantum dots, J. Mater. Chem. C 5 (2017) 8187–8193.
- [21] B.G. Krishna, D.S. Ghosh, S. Tiwari, Tuning optical properties of CsPbBr3 perovskite nanocrystals through silver doping, J. Mater. Sci.: Mater. Electron., (2021) Ahead of Print.
- [22] Y. Zhou, Z. Zhou, M. Chen, Y. Zong, J. Huang, S. Pang, N.P. Padture, Doping and alloying for improved perovskite solar cells, J. Mater. Chem. A 4 (2016) 17623–17635.
- [23] D. Weber, CH3NH3PbX3, ein Pb(II)-System mit kubischer Perowskitstruktur (CH3NH3PbX3, a lead(II) system with cubic perovskite structure), Z. Naturforsch. B 33 (1978) 1443–1445.
- [24] D. Weber, CH3NH3SnBrxl3 x (x = 0-3), ein Sn(II)-System mit kubischer Perowskitstruktur (CH3NH3SnBrxl3-x (x = 0-3), a tin(II) system with a cubic perovskite structure), Z. Naturforsch. B 33 (1978) 862–865.
- [25] K. Chondroudis, D.B. Mitzi, Electroluminescence from an organic-inorganic perovskite incorporating a quaterthiophene dye within lead halide perovskite layers, Chem Mater 11 (1999) 3028–3030.
- [26] A. Kojima, K. Teshima, Y. Shirai, T. Miyasaka, Organometal Halide Perovskites as Visible-Light Sensitizers for Photovoltaic Cells, J. Am. Chem. Soc. 131 (2009) 6050–6051.
- [27] H.S. Kim, C.R. Lee, J.H. Im, K.B. Lee, T. Moehl, A. Marchioro, S.J. Moon, R. Humphry-Baker, J.H. Yum, J.E. Moser, M. Gratzel, N.G. Park, Lead Iodide Perovskite Sensitized All-Solid-State Submicron Thin Film Mesoscopic Solar Cell with Efficiency Exceeding 9%, Sci. Rep. 2 (2012) 591.
- [28] M.M. Lee, J. Teuscher, T. Miyasaka, T.N. Murakami, H.J. Snaith, Efficient Hybrid Solar Cells Based on Meso-Superstructured Organometal Halide Perovskites, Science 338 (2012) 643–647.
- [29] M. Liu, A. Matuhina, H. Zhang, P. Vivo, Advances in the stability of halide perovskite nanocrystals, Materials 12 (2019) 3733.
- [30] Y. Wu, X. Li, H. Zeng, Highly Luminescent and Stable Halide Perovskite Nanocrystals, ACS Energy Lett 4 (2019) 673–681.
- [31] S. Seth, T. Ahmed, A. De, A. Samanta, Tackling the Defects, Stability, and Photoluminescence of CsPbX3 Perovskite Nanocrystals, ACS Energy Lett 4 (2019) 1610–1618.
- [32] L. Protesescu, S. Yakunin, M.I. Bodnarchuk, F. Krieg, R. Caputo, C.H. Hendon, R. X. Yang, A. Walsh, M.V. Kovalenko, Nanocrystals of Cesium Lead Halide Perovskites (CsPbX3, X = Cl, Br, and I): Novel Optoelectronic Materials Showing Bright Emission with Wide Color Gamut, Nano Lett. 15 (2015) 3692–3696.
- [33] Y. Kim, E. Yassitepe, O. Voznyy, R. Comin, G. Walters, X.W. Gong, P. Kanjanaboos, A.F. Nogueira, E.H. Sargent, Efficient Luminescence from Perovskite Quantum Dot Solids, ACS Appl. Mater. Inter. 7 (2015) 25007–25013.
- [34] B.J. Bohn, Y. Tong, M. Gramlich, M.L. Lai, M. Doblinger, K. Wang, R.L.Z. Hoye, P. Muller-Buschbaum, S.D. Stranks, A.S. Urban, L. Polavarapu, J. Feldmann, Boosting Tunable Blue Luminescence of Halide Perovskite Nanoplatelets through Postsynthetic Surface Trap Repair, Nano Lett 18 (2018) 5231–5238.
- [35] K.B. Lin, J. Xing, L.N. Quan, F.P.G. de Arquer, X.W. Gong, J.X. Lu, L.Q. Xie, W. J. Zhao, D. Zhang, C.Z. Yan, W.Q. Li, X.Y. Liu, Y. Lu, J. Kirman, E.H. Sargent, Q. H. Xiong, Z.H. Wei, Perovskite light-emitting diodes with external quantum efficiency exceeding 20 per cent, Nature 562 (2018) 245–248.
- [36] S. Seth, A. Samanta, A Facile Methodology for Engineering the Morphology of CsPbX3 Perovskite Nanocrystals under Ambient Condition, Sci. Rep. 6 (2016) 37693
- [37] V. Neplokh, D.I. Markina, M. Baeva, A.M. Pavlov, D.A. Kirilenko, I.S. Mukhin, A. P. Pushkarev, S.V. Makarov, A.A. Serdobintsev, Recrystallization of CsPbBr3 Nanoparticles in Fluoropolymer Nonwoven Mats for Down- and Up-Conversion of Light, Nanomaterials 11 (2021) 412.
- [38] N. Droseros, G. Longo, J.C. Brauer, M. Sessolo, H.J. Bolink, N. Banerji, Origin of the Enhanced Photoluminescence Quantum Yield in MAPbBr(3) Perovskite with Reduced Crystal Size, ACS Energy Lett 3 (2018) 1458–1466.
- [39] F. Gao, W.Q. Yang, X.L. Liu, Y.Z. Li, W.Z. Liu, H.Y. Xu, Y.C. Liu, Highly stable and luminescent silica-coated perovskite quantum dots at nanoscale-particle level via nonpolar solvent synthesis, Chem. Eng. J. 407 (2021), 128001.
- [40] A.V. Ivanchikhina, K.S. Pundikov, Comparative Study on Methods for the Synthesis of CsPbBr3 Perovskite Nanoparticles at Room Temperature, High Energy Chem 54 (2020) 328–335.
- [41] W. Zhang, Z. Wang, P. Lin, D. Wu, Z. Shi, X. Chen, T. Xu, Y. Tian, X. Li, Controllable synthesis of CsxPbyBrz-based perovskites by a polar solvent-triggered transformation method and its application as an invisible security ink, J. Mater. Sci. 55 (2020) 6826–6833.
- [42] S. Guo, D. Bao, S. Upadhyayula, W. Wang, A.B. Guvenc, J.R. Kyle, H. Hosseinibay, K.N. Bozhilov, V.I. Vullev, C.S. Ozkan, M. Ozkan, Photoinduced Electron Transfer Between Pyridine Coated Cadmium Selenide Quantum Dots and Single Sheet Graphene, Advanced Functional Materials 23 (2013) 5199–5211.
- [43] H. Lu, D. Bao, M. Penchev, M. Ghazinejad, V.I. Vullev, C.S. Ozkan, M. Ozkan, Pyridine-coated lead sulfide quantum dots for polymer hybrid photovoltaic devices, Advanced Science Letters 3 (2010) 101–109.

- [44] S. Gupta, M.R. Chatni, A.L.N. Rao, V.I. Vullev, L.V. Wang, B. Anvari, Virus-mimicking nano-constructs as a contrast agent for near infrared photoacoustic imaging, Nanoscale 5 (2013) 1772–1776.
- [45] S. Upadhyayula, D. Bao, B. Millare, S.S. Sylvia, K.M.M. Habib, K. Ashraf, A. Ferreira, S. Bishop, R. Bonderer, S. Baqai, X. Jing, M. Penchev, M. Ozkan, C. S. Ozkan, R.K. Lake, V.I. Vullev, Permanent Electric Dipole Moments of Carboxyamides in Condensed Media: What Are the Limitations of Theory and Experiment? J. Phys. Chem. B 115 (2011) 9473–9490.
- [46] J.M. Larsen-Clinton, E.M. Espinoza, M.F. Mayther, J. Clark, C. Tao, D. Bao, C. M. Larino, M. Wurch, S. Lara, V.I. Vulley, Fluorinated aminoanthranilamides: non-native amino acids for bringing proteomic approaches to charge-transfer systems, Phys. Chem. Chem. Phys. 19 (2017) 7871–7876.
- [47] S. Upadhyayula, V. Nunez, E.M. Espinoza, J.M. Larsen, D. Bao, D. Shi, J.T. Mac, B. Anvari, V.I. Vullev, Photoinduced dynamics of a cyanine dye: parallel pathways of non-radiative deactivation involving multiple excited-state twisted transients, Chem. Sci. 6 (2015) 2237–2251.
- [48] B. Bahmani, S. Gupta, S. Upadhyayula, V.I. Vullev, B. Anvari, Effect of polyethylene glycol coatings on uptake of indocyanine green loaded nanocapsules by human spleen macrophages in vitro, J. Biomed. Opt. 16 (2011), 051303/ 051301-051303/051310.
- [49] J.T. Mac, V. Nuñez, J.M. Burns, Y.A. Guerrero, V.I. Vullev, B. Anvari, Erythrocyte-derived nano-probes functionalized with antibodies for targeted near infrared fluorescence imaging of cancer cells, Biomed. Opt. Express 7 (2016) 1311–1322.
- [50] J.N. Demas, G.A. Crosby, Measurement of Photoluminescence Quantum Yields -Review, J. Phys. Chem. 75 (1971) 991. -&.
- [51] R. Sjoback, J. Nygren, M. Kubista, Absorption and Fluorescence Properties of Fluorescein, Spectrochim. Acta A 51 (1995) L7–L21.
- [52] M.M. Martin, L. Lindqvist, The pH dependence of fluorescein fluorescence, J. Lumin. 10 (1975) 381–390.
- [53] J. Wan, A. Ferreira, W. Xia, C.H. Chow, K. Takechi, P.V. Kamat, G. Jones, V. I. Vullev, Solvent dependence of the charge-transfer properties of a quaterthiophene-anthraquinone dyad, J. Photochem. Photobiol., A 197 (2008) 364–374.
- [54] G. Jones II, V.I. Vullev, Medium effects on the photophysical properties of terbium (III) complexes with pyridine-2,6-dicarboxylate, Photochem. Photobiol. Sci. 1 (2002) 925–933.
- [55] G. Jones II, V.I. Vullev, Medium Effects on the Stability of Terbium(III) Complexes with Pyridine-2,6-dicarboxylate, J. Phys. Chem. A 106 (2002) 8213–8222.
- [56] D.F. Eaton, Recommended methods for fluorescence decay analysis, Pure Appl. Chem. 62 (1990) 1631–1648.
- [57] K. Pearson, On the Criterion that a given System of Deviations from the Probable in the Case of a Correlated System of Variables is such that it can be reasonably supposed to have arisen from Random Sampling, The London, Edinburgh, and Dublin Philosophical Magazine, and, Journal of Science 50 (1900) 157–175.

- [58] J. Durbin, G.S. Watson, Testing for Serial Correlation in Least Squares Regression .3, Biometrika 58 (1971) 1. -&.
- [59] J. Durbin, G.S. Watson, Testing for Serial Correlation in Least Squares Regression .2, Biometrika 38 (1951) 159–178.
- [60] J. Durbin, G.S. Watson, Testing for Serial Correlation in Least Squares Regression .1., Biometrika, 37 (1950) 409-428.
- [61] G. Ángulo, G. Grampp, A. Rosspeintner, Recalling the appropriate representation of electronic spectra, Spectrochim. Acta A 65 (2006) 727–731.
- [62] J. De Roo, M. Ibanez, P. Geiregat, G. Nedelcu, W. Walravens, J. Maes, J.C. Martins, I. Van Driessche, M.V. Kovalenko, Z. Hens, Highly Dynamic Ligand Binding and Light Absorption Coefficient of Cesium Lead Bromide Perovskite Nanocrystals, ACS Nano 10 (2016) 2071–2081.
- [63] M. Krzeszewski, E.M. Espinoza, C. Cervinka, J.B. Derr, J.A. Clark, D. Borchardt, G. J.O. Beran, D.T. Gryko, V.I. Vullev, Dipole Effects on Electron Transfer are Enormous, Angew. Chem., Int. Ed. 57 (2018) 12365–12369.
- [64] M. Tachiya, Application of a generating function to reaction kinetics in micelles. Kinetics of quenching of luminescent probes in micelles, Chem. Phys. Lett. 33 (1975) 289–292.
- [65] M. Tachiya, Kinetics of Quenching of Luminescent Probes in Micellar Systems. II, J Chem Phys 76 (1982) 340–348.
- [66] R. Koole, B. Luigjes, M. Tachiya, R. Pool, T.J.H. Vlugt, C.D.M. Donega, A. Meijerink, D. Vanmaekelbergh, Differences in cross-link chemistry between rigid and flexible dithiol molecules revealed by optical studies of CdTe quantum dots, J. Phys. Chem. C 111 (2007) 11208–11215.
- [67] S. Sadhu, M. Tachiya, A. Patra, A Stochastic Model for Energy Transfer from CdS Quantum Dots/Rods (Donors) to Nile Red Dye (Acceptors), J. Phys. Chem. C 113 (2009) 19488–19492.
- [68] V.V. Matylitsky, L. Dworak, V.V. Breus, T. Basche, J. Wachtveitl, Ultrafast Charge Separation in Multiexcited CdSe Quantum Dots Mediated by Adsorbed Electron Acceptors, J. Am. Chem. Soc. 131 (2009) 2424–2425.
- [69] N.H. Song, H.M. Zhu, S.Y. Jin, W. Zhan, T.Q. Lian, Poisson-Distributed Electron-Transfer Dynamics from Single Quantum Dots to C60 Molecules, ACS Nano 5 (2011) 613–621.
- [70] K.E. Knowles, M. Malicki, E.A. Weiss, Dual-Time Scale Photoinduced Electron Transfer from PbS Quantum Dots to a Molecular Acceptor, J. Am. Chem. Soc. 134 (2012) 12470–12473.
- [71] M. Mittal, S. Sapra, Nanocrystal-Dye Interactions: Studying the Feasibility of Co-Sensitization of Dyes with Semiconductor Nanocrystals, ChemPhysChem 18 (2017) 2509–2516.
- [72] S. Mandal, L. George, N.V. Tkachenko, Charge transfer dynamics in CsPbBr3 perovskite quantum dots-anthraquinone/fullerene (C-60) hybrids, Nanoscale 11 (2019) 862–869.